metals

MDPI

Article

Effects of Heat Treatment and Deformation on Microstructure and Properties of Cu–Ni–Si Alloy/AA8030 Alloy Composite Wires

Shuke Tian [1,2], Fan Zhao [1,2,3,*] and Xinhua Liu [1,2,4,*]

[1] Key Laboratory for Advanced Materials Processing (MOE), Institute for Advanced Materials and Technology, University of Science and Technology Beijing, Beijing 100083, China; b20190618@xs.ustb.edu.cn
[2] Beijing Laboratory of Metallic Materials and Processing for Modern Transportation, Institute for Advanced Materials and Technology, University of Science and Technology Beijing, Beijing 100083, China
[3] Institute of Materials Intelligent Technology, Liaoning Academy of Materials, Shenyang 110167, China
[4] Institute of Materials Genome Engineering, Henan Academy of Sciences, Zhengzhou 450046, China
* Correspondence: zhaofan@ustb.edu.cn (F.Z.); liuxinhua@ustb.edu.cn (X.L.)

Abstract: The influence of heat treatment and deformation on the microstructure and properties of a Cu–Ni–Si alloy/AA8030 alloy composite wire was studied. After aging at 450 °C for 60 min, the composite wire exhibited relatively high comprehensive properties, with ultimate tensile strength, elongation, and electrical conductivity values of 253 MPa, 11.1%, and 55.3% IACS, respectively. Microstructural analysis revealed that precipitation and dislocation strengthening played important roles in the aged Cu–Ni–Si alloy cladding, whereas grain boundary and dislocation strengthening contributed to the strength of the AA8030 alloy. Then, the wire underwent five passes of drawing with a total deformation of 75%. Significant work hardening changed the ultimate tensile strength, elongation, and electrical conductivity of the composite wire to 422 MPa, 3.3%, and 53.6% IACS, respectively. $CuAl_2$, CuAl and Cu_9Al_4 layers were formed at the composite interface during aging. The $CuAl_2$ and Cu_9Al_4 layers grew toward the Al alloy and Cu alloy, respectively, whereas the CuAl layer grew toward both the Al alloy and the Cu alloy.

Keywords: Cu/Al composite; composite wire; Cu–Ni–Si alloy; AA8030 alloy; composite interface

Citation: Tian, S.; Zhao, F.; Liu, X. Effects of Heat Treatment and Deformation on Microstructure and Properties of Cu–Ni–Si Alloy/AA8030 Alloy Composite Wires. *Metals* **2024**, *14*, 1330. https://doi.org/10.3390/met14121330

Academic Editor: Frank Czerwinski

Received: 30 October 2024
Revised: 21 November 2024
Accepted: 21 November 2024
Published: 24 November 2024

1. Introduction

Layered Cu/Al composites, which combine the advantages of Cu and Al, such as light weight, low cost, and good thermal and electrical conductivity, have been employed in a wide range of applications, including power transmission and heat transfer equipment [1–3]. Using a Cu/Al composite to replace pure Cu or Cu alloy conductors in aircraft is of great importance for reducing the weight of aerospace power systems while also promoting the overall design and application development of aerospace equipment. However, the advancement of aerospace technology and the more severe service environment in that field have placed greater demands on the mechanical properties of conductor materials, such as strength and creep resistance [4–7]. The development of a novel Cu alloy/Al alloy composite is a viable solution to the aforementioned challenges.

Cu–Ni–Si alloys are utilized for electrical components because of their high electrical conductivity and strength [8–11]. The AA8030 aluminum alloy is used for electrical conductors because of its good strength, electrical conductivity and creep resistance [12–15]. Compared with pure Cu/pure Al composites, these two types of materials can improve the properties of composites. The strength and electrical conductivity of Cu–Ni–Si alloys are usually improved by solution and aging treatments, but the solution temperatures of Cu–Ni–Si alloys are higher than the melting point of the AA8030 alloy, so composites of these alloys cannot be solution-treated. To solve the above problems, the authors developed

a compositional design for Cu–Ni–Si alloy cladding and fabricated a Cu–Ni–Si alloy-clad AA8030 alloy composite via continuous casting composite technology [16]. Owing to the strong cooling effect of continuous casting, the second-phase precipitation of the Cu–Ni–Si alloy during solidification was suppressed, and a good solid solution effect was obtained after casting, allowing us to eliminate the solid solution treatment. This was reported in our previous work [16].

Moreover, Cu–Ni–Si alloys are age-hardened copper alloys in which fine and dispersed precipitated phases are formed after aging treatment, giving these alloys excellent strength, elasticity, electrical conductivity, and stress relaxation resistance, and the aging temperatures for Cu–Ni–Si alloys generally range from 400 °C to 500 °C [17,18]. Considering that the AA8030 alloy is a work-hardened Al alloy, its microstructure and properties need to be regulated through deformation and annealing treatments, and the annealing temperature for the AA8030 alloy typically ranges from 250 °C to 350 °C [19]. The difference in these heat treatment temperatures poses a significant challenge in the preparation of high-performance Cu–Ni–Si alloy/AA8030 alloy composites. As a result, it is crucial to clarify the effects of aging and deformation on the overall microstructure and properties of Cu–Ni–Si alloy/AA8030 alloy composites.

This study focuses on Cu–Ni–Si alloy-clad AA8030 alloy composite wires prepared by continuous composite casting, rolling and drawing, and studies the effects of deformation and heat treatment parameters on the microstructure, interfacial layers, and properties of these composite wires. Furthermore, the evolution mechanisms of the mechanical and electrical properties of the composite wires are explored, offering fundamental theoretical guidance for the development and preparation of high-performance Cu alloy/Al alloy composite materials.

2. Materials and Methods

2.1. Material Preparation

Cu–Ni–Si alloy/AA8030 alloy composite wires were prepared by continuous composite casting, groove rolling and drawing, and the density value for the composites was 4.94 g/cm^3. The AA8030 alloy used was a commercially available alloy, and Cu–Ni–Si alloy was prepared by combining pure Cu, pure Ni, and pure Si in a vacuum melting furnace. Due to the strong cooling effect of continuous casting composite technology, the as-cast Cu–Ni–Si alloy had a good solution effect [16], and the Cu–Ni–Si alloy could be aged without solution-treatment. The preparation process was as follows: a Cu–Ni–Si alloy/AA8030 alloy composite billet with a diameter of 20 mm and a cladding thickness of 2 mm was prepared via the continuous casting composite technology reported in reference [16], as shown in Figure 1a,b; subsequently, the composite billet was processed through 8 passes of groove rolling and 11 passes of drawing to obtain a composite wire with a diameter of 2 mm and a cladding thickness of 0.2 mm, as illustrated in Figure 1c and d. The composition of Cu–Ni–Si alloy and AA8030 alloy were confirmed by inductively coupled plasma-optical emission spectrometry, as shown in Table 1.

Table 1. Chemical compositions of the Cu–Ni–Si alloy and the AA8030 alloy (wt.%).

Alloy	Cu	Al	Ni	Si	Mg	Fe	Zn
Cu–Ni–Si	Bal.	—	1.00 ± 0.02	0.23 ± 0.02	—	—	—
AA8030	0.23 ± 0.02	Bal.	—	0.04 ± 0.01	0.05 ± 0.01	1.00 ± 0.01	0.02 ± 0.01

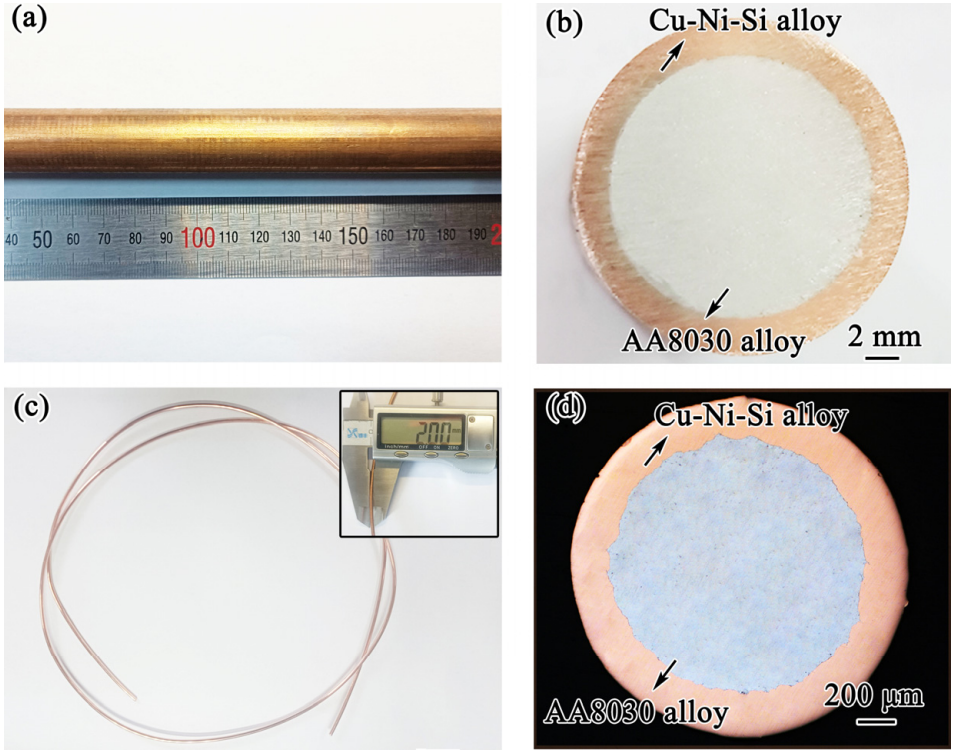

Figure 1. The Cu–Ni–Si alloy-clad AA8030 alloy composite rod (**a**) and its cross section (**b**) after continuous casting composite technology; the Cu–Ni–Si alloy-clad AA8030 alloy composite wire (**c**) and its cross section (**d**) after groove rolling and drawing.

2.2. Experimental Procedure

Cu–Ni–Si alloys are age-hardened copper alloys, and the strength and electrical conductivity of Cu–Ni–Si alloys are usually improved by aging treatment. First, in order to improve the properties of the Cu–Ni–Si alloy, the composite wires were subjected to aging in a chamber furnace at temperatures of 400 °C and 450 °C for durations ranging from 15 to 120 min. Then, in order to further improve the strength of the AA8030 alloy, the wires that underwent the optimized aging process were subjected to cold drawing to improve their strength. The drawing process involved a total of 5 passes, with a diameter reduction of 0.2 mm in each pass.

2.3. Characterization and Testing

The grain morphology of the Al alloy was observed via electron backscattered diffraction (EBSD) on a JEM-7900F scanning electron microscope (SEM) (JEOL, Akishima, Japan) with a scanning voltage of 20 kV and a scanning step length of 0.05 μm. Data processing was performed via the HKL Channel 5 system. The microstrains of the Cu alloy and Al alloy were evaluated by XRD analysis via a TTRIII X-ray diffractometer (Rigaku, Akishima, Japan) with a scanning angle range of 20–100° and a scanning rate of 6°/min, and all data were collected using Kα radiation. A JEM-7900F SEM (JEOL, Akishima, Japan) equipped with an energy dispersive spectrometer (EDS) was used to analyze the interface structure of the composite wire. A JXA-8530F Plus electron probe microanalyzer (EPMA) (JEOL, Akishima, Japan), operated at an acceleration voltage of 15 kV and a probe current of 10 nA, was used to investigate the elemental distributions at the composite interface. TEM samples were prepared via a ThermoFisher Scios-2 dual-beam electron microscope (Waltham, MA, USA). The process for preparing the TEM samples was as follows: samples with a length of approximately 12 μm, a width of approximately 6 μm, and a thickness of approximately 1.5–2.0 μm were lifted from the region of interest via an ion beam with a voltage of 30 kV and a current of 80–2000 pA; then, each sample was thinned to electron transparency (100–150 nm) via a voltage of 30 kV and a current of 0.1 nA. The microstructures of the

Cu alloy, Al alloy and composite interface were analyzed via transmission electron microscopy (TEM) with a Thermo Fisher Talos F200X G2 instrument (Waltham, MA, USA) at an accelerating voltage of 200 kV.

Hardness testing was conducted with a VTD512 Vickers microhardness tester (LEICA, Wetzlar, Germany) with a load of 100 g and a dwell time of 15 s. Five measurements from different areas of each sample were recorded, and the average value was calculated. The ultimate tensile strength of the composite wires was tested at 0.5 mm/min via a CTM2500 material testing machine, the length of the wires was 150 mm, and the gauge length was 100 mm. Three samples for each condition were tested, and the average values of the properties were calculated to obtain the test results. The room temperature electrical conductivity of each composite wire was tested via an Applent AT-516-type precision DC resistance tester (Applent, Changzhou, China), and the length of the sample was 100 mm. The measurement was repeated 5 times for each sample to obtain an average value.

3. Results

3.1. Evolution of the Microstructure and Properties During the Aging Process

Figure 2 shows IPF maps of the longitudinal section of the AA8030 alloy after heat treatment at 400 °C and 450 °C for 15–120 min. After heat treatment at 400 °C and 450 °C for 15 min, the deformed microstructure of the AA8030 alloy completely disappeared and was replaced by a recrystallized microstructure, indicating that the degree of softening reached its maximum. As the heat treatment temperature increased from 400 °C to 450 °C, the average diameter of the grains increased from approximately 9 μm to 13 μm. However, as the heat treatment time increased from 15 min to 120 min at 400 °C and 450 °C, the average grain diameter did not increase significantly.

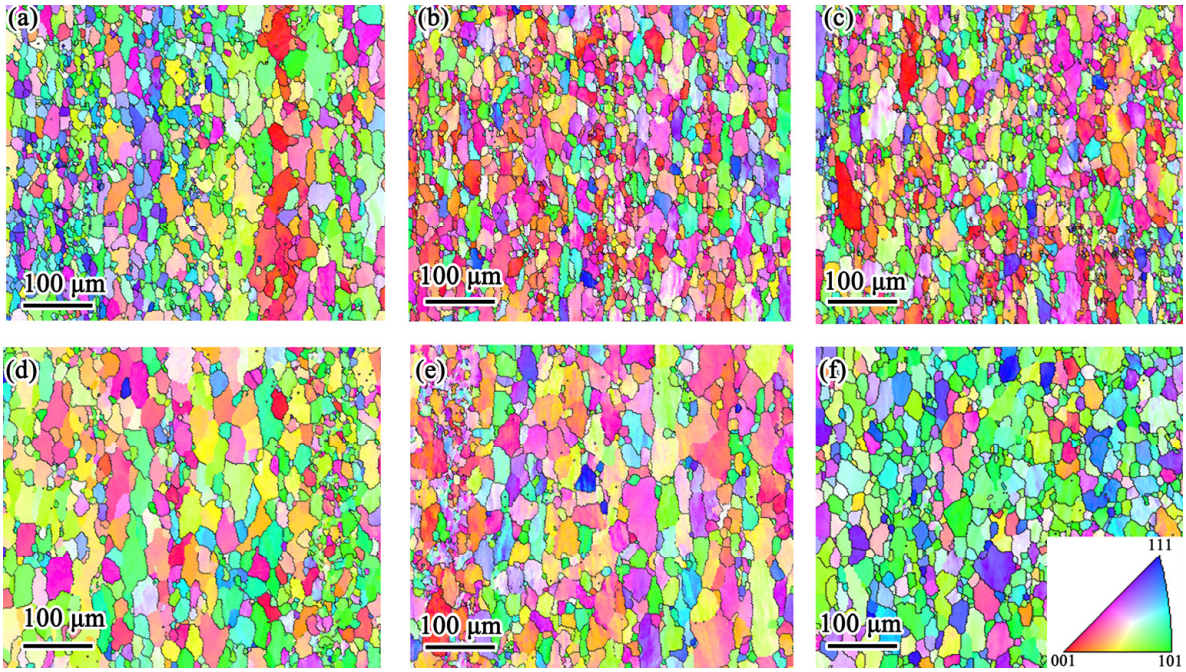

Figure 2. The IPF maps of the longitudinal section of the AA8030 alloy after heat treatment; the black lines represent grain boundaries (>15°): (**a**) 400 °C, 15 min; (**b**) 400 °C, 60 min; (**c**) 400 °C, 120 min; (**d**) 450 °C, 15 min; (**e**) 450 °C, 60 min; (**f**) 450 °C, 120 min.

Figure 3a shows the TEM morphology of the Cu–Ni–Si alloy before aging. High-density dislocations were produced inside the Cu–Ni–Si alloy because of the deformation caused by rolling and drawing during the preparation of the composite wires. As shown in Figure 3b, obvious recovery occurred, and the dislocation density decreased sharply when the composite wire was aged at 450 °C for 15 min. As shown in Figure 3c, precipitate

phases with an average size of approximately 7.2 nm formed within the Cu–Ni–Si alloy when the composite wire was aged at 450 °C for 60 min. The precipitate phase can be identified as the Ni_2Si phase with an orthorhombic structure and lattice constants a = 0.706 nm, b = 0.499 nm, and c = 0.372 nm. As shown in Figure 3d, the Ni_2Si precipitates were coarsened to approximately 50 nm, and long rod-shaped precipitates with lengths of approximately 200 nm formed within the Cu–Ni–Si alloy when the composite wire was aged at 450 °C for 120 min. The rod-shaped precipitates can be identified as the Ni_2Si phase. Additionally, subgrain structures formed within the Cu–Ni–Si alloy when the composite wire was aged at 450 °C for 120 min. During the aging process, the rearrangement of dislocations led to the formation of dislocation walls. During the recovery process, these dislocation walls evolved into low-angle grain boundaries and subsequently transformed into subgrain boundaries.

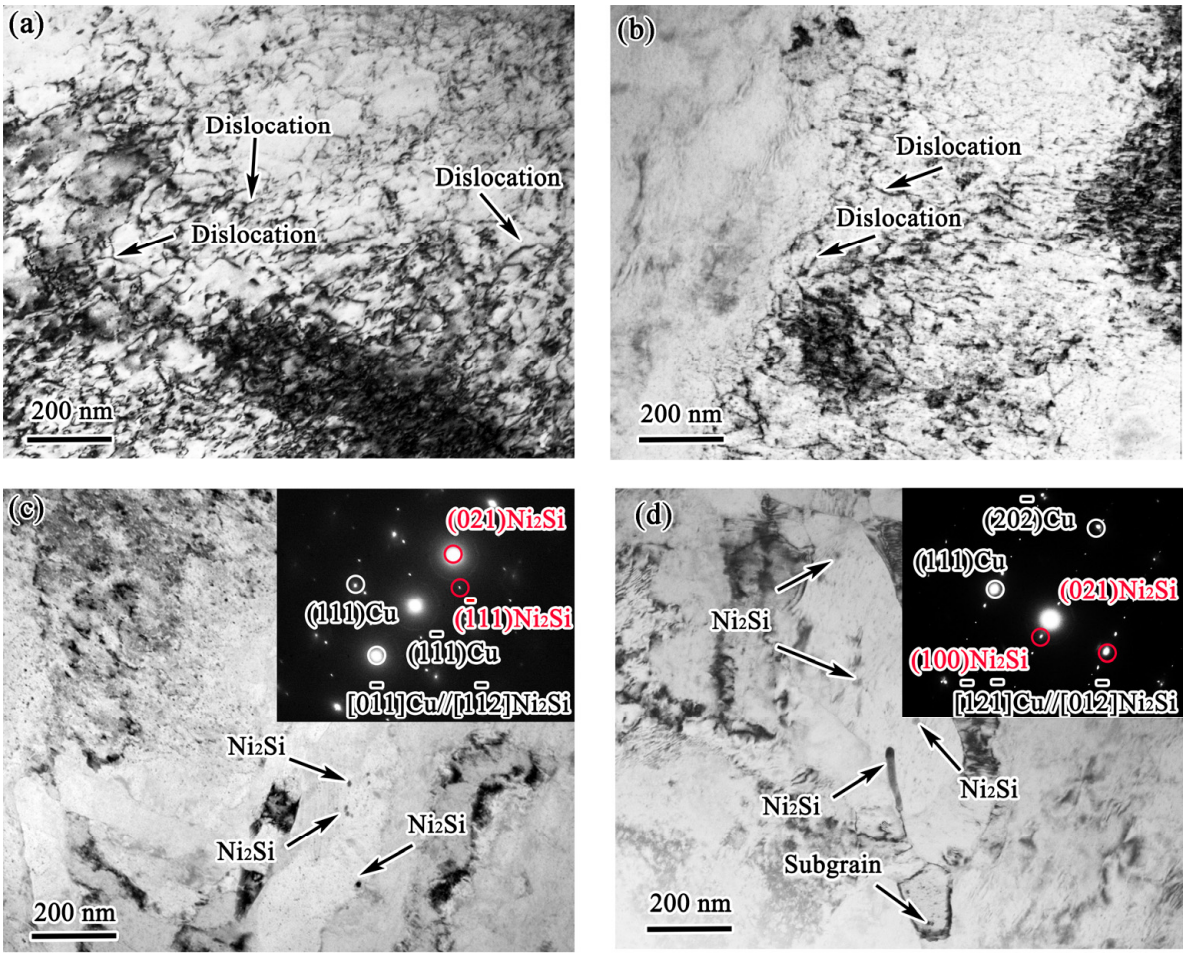

Figure 3. TEM micrographs of Cu–Ni–Si alloy after aging at 450 °C for various durations: (**a**) 0 min; (**b**) 15 min; (**c**) 60 min; (**d**) 120 min.

Figure 4 shows SEM images of the interface of the composite wire after heat treatment at 400 °C and 450 °C for 15–120 min. After aging at 400 °C and 450 °C for 15–120 min, three interface layers formed at the interface of the composite wire. When the aging temperature was 400 °C, as the aging time increased from 15 to 120 min, the thickness of the interface layer gradually increased from 3.7 μm to 9.5 μm. When the aging temperature was 450 °C, as the aging time increased from 15 to 120 min, the thickness of the interface layer gradually increased from 4.6 μm to 17.8 μm. To distinguish the three interface layers, EDS quantitative analysis was performed, and the results are shown in Table 2. Many studies [2–5] have shown that Cu_9Al_4, CuAl, and $CuAl_2$ were formed in the Cu-Al composite interface during solid diffusion. The EDS quantitative analysis in Table 2 is consistent with previous

research [2–5], thus it can be determined that the interface layer is composed of Cu_9Al_4, CuAl, and $CuAl_2$ layers.

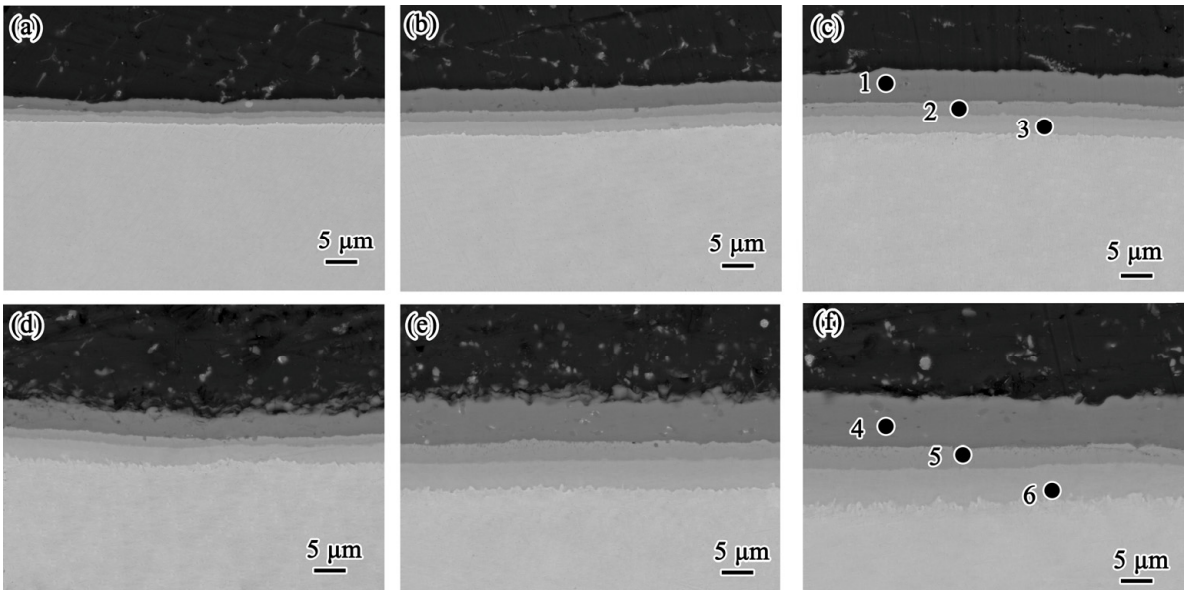

Figure 4. SEM images of the interface of the composite wire after aging at 400 °C and 450 °C for 15–120 min: (**a**) 400 °C, 15 min; (**b**) 400 °C, 60 min; (**c**) 400 °C, 120 min; (**d**) 450 °C, 15 min; (**e**) 450 °C, 60 min; (**f**) 450 °C, 120 min.

Table 2. EDS results for the interfacial phases in Figure 4.

	1	**2**	**3**	**4**	**5**	**6**
Al (at.%)	65.2	49.8	32.9	67.5	52.9	31.9
Cu (at.%)	34.1	50.2	67.1	32.5	47.1	68.1
Interfacial phase	$CuAl_2$	CuAl	Cu_9Al_4	$CuAl_2$	CuAl	Cu_9Al_4

Figure 5a shows the variations in the hardness of the AA8030 alloy after annealing at 400–450 °C for various durations. After groove rolling and drawing, the hardness of the AA8030 alloy was 111.1 HV. The hardness of the AA8030 alloy decreased to approximately 40 HV when the composite wire was heated at 450 °C for 15 to 120 min. As the annealing temperature increased from 400 °C to 450 °C, the decrease in the average diameter of the AA8030 alloy was insignificant, resulting in the hardness of the AA8030 alloy remaining at approximately 40 HV during the annealing process. Figure 5b shows the variations in the hardness of the Cu–Ni–Si alloy after aging at 400–450 °C for various durations. After groove rolling and drawing, the hardness of the Cu–Ni–Si alloy was 140.3 HV. When the composite wire was aged at 400 °C for 15 min, the hardness of the Cu–Ni–Si alloy decreased to 116.4 HV. However, when the composite wire was aged at 400 °C for 30 to 120 min, the hardness increased to approximately 126 HV. When the composite wire was aged at 450 °C for 15 min, the hardness of the Cu–Ni–Si alloy decreased to 126.3 HV. However, when the composite wire was aged at 450 °C for 60 to 120 min, the hardness increased to approximately 150 HV. As shown in Figure 3a,b, the sharp decrease in dislocation density led to a decrease in the hardness of the Cu–Ni–Si alloy when the composite wire was aged at 450 °C for 15 min. As shown in Figure 3c, Ni_2Si phases with an average size of approximately 7.2 nm formed, and the precipitation strengthening effect enhanced the strength of the Cu–Ni–Si alloy when the composite wire was aged at 450 °C for 60 to 120 min.

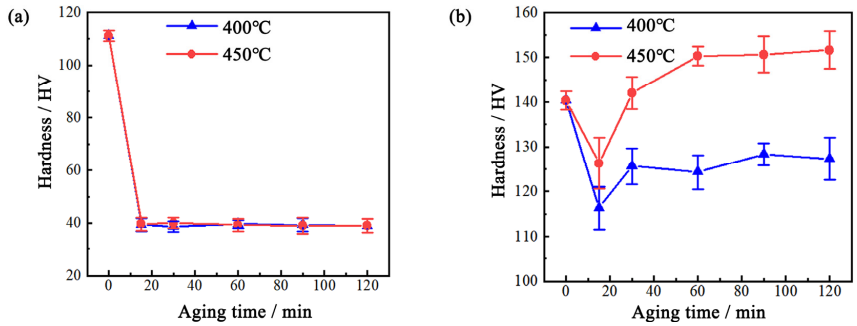

Figure 5. The hardness of (**a**) AA8030 alloy and (**b**) Cu–Ni–Si alloy after aging at 400–450 °C for different durations.

The strength of the Cu–Ni–Si alloy was also affected by dislocation strengthening and precipitation strengthening. During the aging process, a decrease in the dislocation density led to a decrease in the strength of the alloy. However, precipitation strengthening resulted in an increase in the strength of the alloy. When the Cu alloy was aged at 400 °C, the increase in strength due to precipitation strengthening was less than the decrease caused by the reduction in dislocation strengthening, resulting in an overall decrease in the strength of the alloy. When the Cu alloy was aged at 450 °C for 60 to 120 min, the increase in strength from precipitation strengthening exceeded the decrease due to the reduction in dislocation strengthening, leading to an overall increase in the strength of the alloy. In conclusion, the optimal aging temperature for the composite wire was 450 °C.

Figure 6 shows the variations in the ultimate tensile strength, elongation and electrical conductivity of the Cu–Ni–Si/AA8030 composite wire after being aged at 450 °C for 15–120 min. The ultimate tensile strength and elongation of the composite wire gradually increased when it was aged at 450 °C for 15 to 60 min. The ultimate tensile strength and elongation remained stable when it was aged at 450 °C for 60 to 90 min. However, the ultimate tensile strength and elongation of the composite wire decreased when it was aged at 450 °C for 90 to 120 min. Additionally, as the aging time increased, the electrical conductivity of the composite wire gradually increased. In summary, the optimal aging process for the Cu–Ni–Si/AA8030 composite wire was aging at 450 °C for 60 min, which resulted in ultimate tensile strength, elongation, and electrical conductivity values of 253 MPa, 11.1%, and 55.3% IACS, respectively.

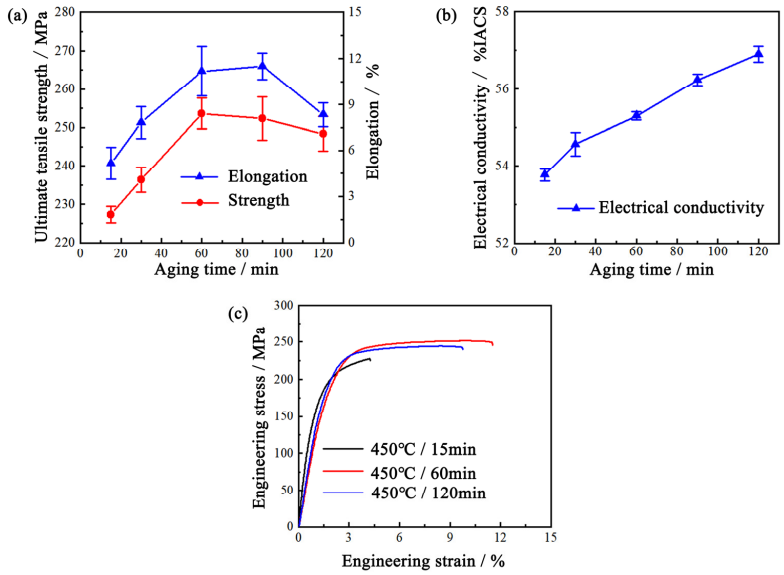

Figure 6. (**a**) Ultimate tensile strength, elongation, (**b**) electrical conductivity and (**c**) engineering stress–engineering strain curves of the composite wires after aging at 450 °C for different durations.

The strength of composite wires is influenced by the properties of the matrix alloy and the thickness of the interface layer. Research has shown [20] that an increase in the thickness of the interface layer is detrimental to the mechanical properties of Cu–Al composites. When the composite wire was aged at 450 °C for 15 to 60 min, the thickness of the interface layer gradually increased to approximately 10 μm, the hardness of the Al alloy was approximately 40 HV, the hardness of the Cu alloy gradually increased from 126 HV to 150.3 HV, and the ultimate tensile strength of the composite wire progressively increased to 253 MPa. Therefore, the strengthening of the Cu alloy was the primary factor contributing to the increased strength of the composite wire when the composite wire was aged at 450 °C for 15 to 60 min. As the aging time increased from 60 min to 120 min, the thickness of the interface layer gradually increased from approximately 10 μm to approximately 18 μm, the hardness of the Al alloy was approximately 40 HV, the hardness of the Cu alloy was approximately 150 HV, and the ultimate tensile strength of the composite wire progressively decreased from 253 MPa to 248 MPa. Therefore, the thickness of the interface layer was the primary factor contributing to the reduction in the strength of the composite wire when the composite wire was aged at 450 °C for 60 to 120 min.

3.2. Evolution of the Microstructure and Properties During the Drawing Process

Figure 7 presents TEM images of the AA8030 alloy during the drawing deformation process. After deformation, the microstructure of the AA8030 alloy was composed of polygonal dislocation cells and dislocation walls. The dislocation walls were formed by entangled dislocations, and dislocations of varying sizes can be observed in the dislocation cells. As the deformation increased, the size of the dislocation cells gradually decreased, whereas the dislocation density gradually increased.

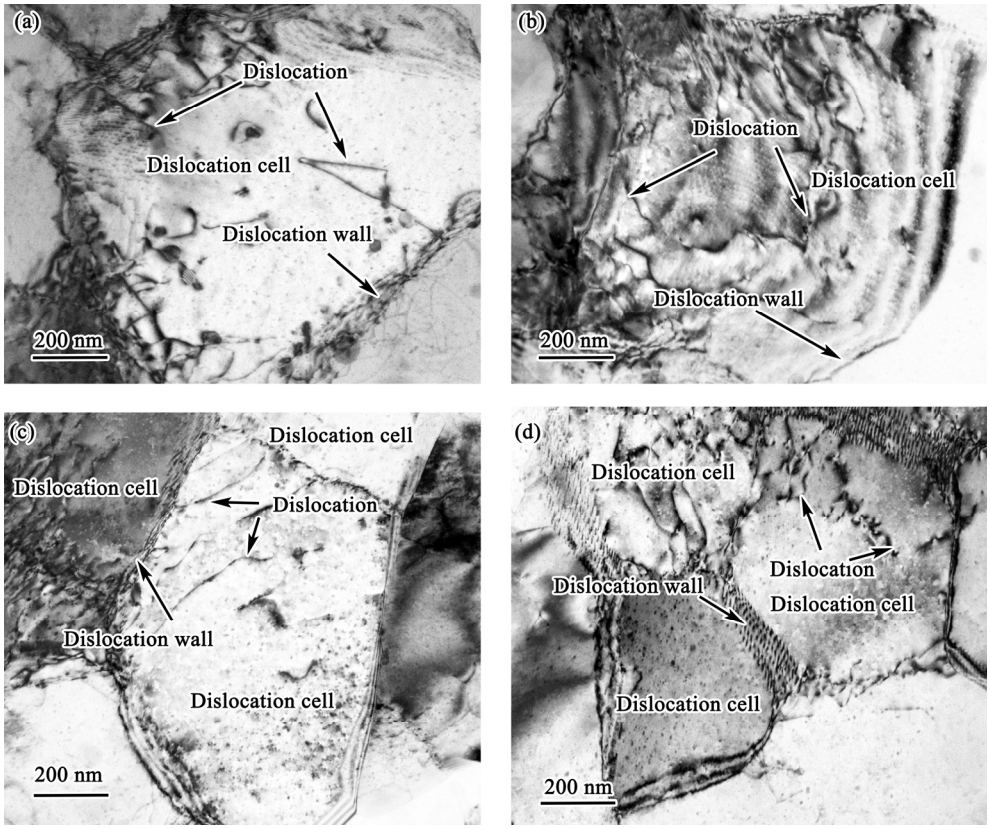

Figure 7. TEM bright-field images of AA8030 alloy after different numbers of passes of drawing deformation: (**a**) two passes, with a deformation of 36%; (**b**) three passes, with a deformation of 51%; (**c**) four passes, with a deformation of 64%; (**d**) five passes, with a deformation of 75%.

Figure 8 shows TEM bright-field images of the Cu–Ni–Si alloy after different numbers of passes of drawing deformation. After two passes of drawing deformation (with a deformation of 36%), dislocation cells formed within the Cu–Ni–Si alloy. The dislocation walls were composed of entangled dislocations, as shown in Figure 8a. After three passes of drawing deformation (with a deformation of 51%), the dislocation cells were elongated along the drawing direction, and band structures with high dislocation densities formed, as shown in Figure 8b. After four passes of drawing deformation (with a deformation of 64%), the number of band structures increased, with a distance of approximately 500 nm between two adjacent band structures, as shown in Figure 8c. After five passes of drawing deformation (with a deformation of 75%), the number of band structures further increased. The width of the band structures was approximately 100 nm, with a distance of approximately 200 nm between two adjacent band structures, as shown in Figure 8d.

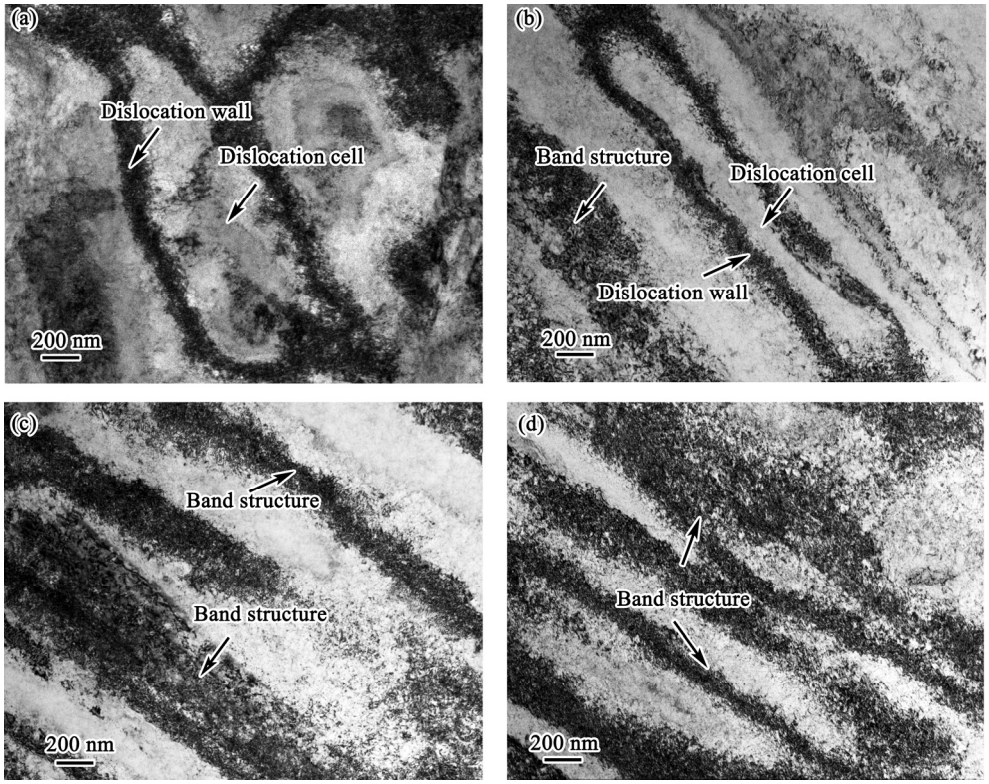

Figure 8. TEM bright-field images of Cu–Ni–Si alloy after different numbers of passes of drawing deformation: (**a**) two passes, with a deformation of 36%; (**b**) three passes, with a deformation of 51%; (**c**) four passes, with a deformation of 64%; (**d**) five passes, with a deformation of 75%.

Figure 9 presents SEM images of the interface of the composite wire after different numbers of passes of drawing deformation. After two passes of drawing deformation (with a deformation of 36%), brittle fracture occurred in the interface layer, and new bonds formed, as shown in Figure 9a. As the deformation increased, the new bonds gradually expanded, and the angle between the fractured intermetallic compounds and the drawing direction gradually increased, as shown in Figure 9b–d. The angle between the fractured interfacial layer and the drawing direction was caused by the pressure applied by the mold.

Figure 10 shows the variations in hardness for the AA8030 alloy and the Cu–Ni–Si alloy after different numbers of passes of drawing deformation. As the deformation increased, the hardness of the AA8030 alloy and the Cu–Ni–Si alloy gradually improved. After five passes of drawing deformation (with a deformation of 75%), the hardness of the AA8030 alloy reached 101.3 HV, and the hardness of the Cu–Ni–Si alloy reached 171.6 HV.

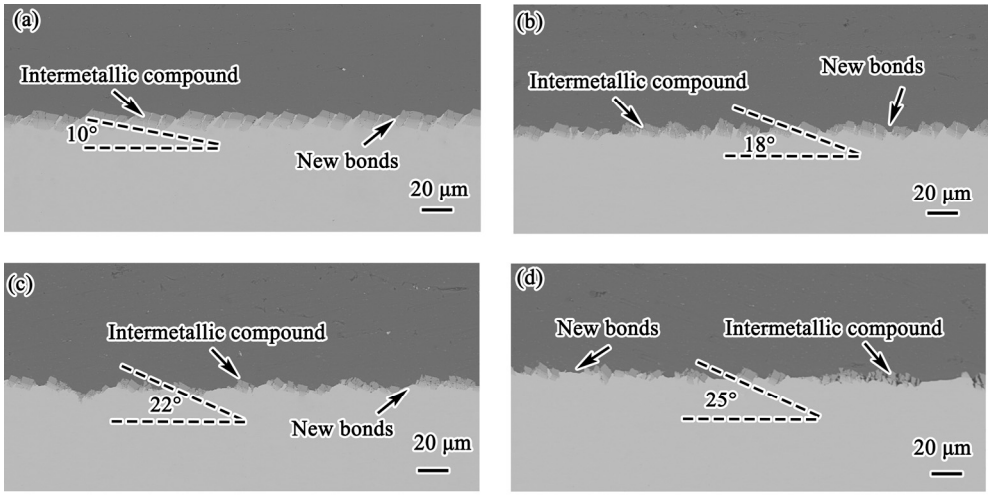

Figure 9. SEM images of the interface of the composite wire after different numbers of passes of drawing deformation: (**a**) two passes, with a deformation of 36%; (**b**) three passes, with a deformation of 51%; (**c**) four passes, with a deformation of 64%; (**d**) five passes, with a deformation of 75%.

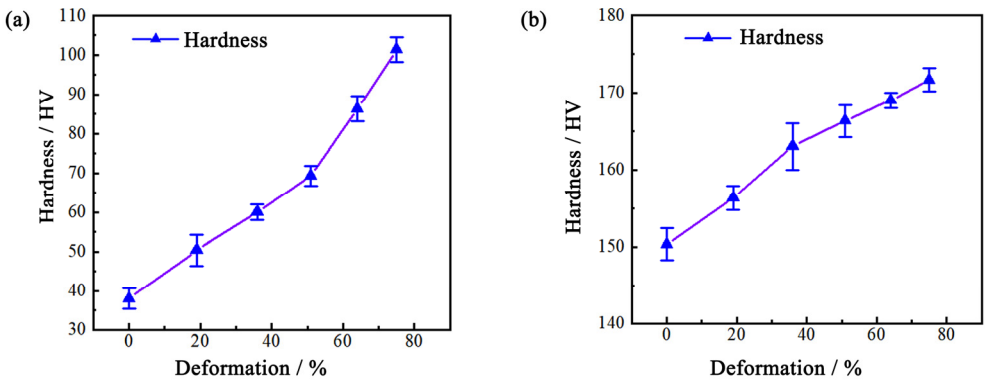

Figure 10. The variations in hardness for (**a**) AA8030 alloy and (**b**) Cu–Ni–Si alloy after different numbers of passes of drawing deformation.

The mechanical properties of the AA8030 alloy are closely related to its microstructure. During plastic deformation, many dislocations formed within the alloy, leading to the creation of dislocation cells and dislocation walls, which hindered the movement of dislocations and subsequently increased the strength of the Al alloy. As the deformation increased, the size of the dislocation cells gradually decreased, and the dislocation strengthening effect significantly improved. During the drawing deformation process, band structures with high dislocation density formed within the Cu–Ni–Si alloy. The band structures divided the Cu alloy into multiple regions, which hindered the movement of dislocations and thus enhanced the strength of the Cu–Ni–Si alloy. As the deformation increased, the dislocation strengthening effect significantly improved.

Figure 11 shows the variations in the ultimate tensile strength, elongation and electrical conductivity of the Cu–Ni–Si/AA8030 composite wires after different numbers of drawing deformation passes. As the deformation increased, the ultimate tensile strength gradually increased, whereas the electrical conductivity and elongation gradually decreased. After five drawing passes (with a deformation of 75%), the ultimate tensile strength, elongation and electrical conductivity of the composite wire were 422 MPa, 3.3%, and 53.6% IACS, respectively. On the basis of the above analysis results, during the drawing deformation process, the properties of the AA8030 and Cu–Ni–Si alloys directly influenced the performance of the composite wire. The greater the deformation was, the more significant the work hardening effect, and the greater the strength of the composite wire.

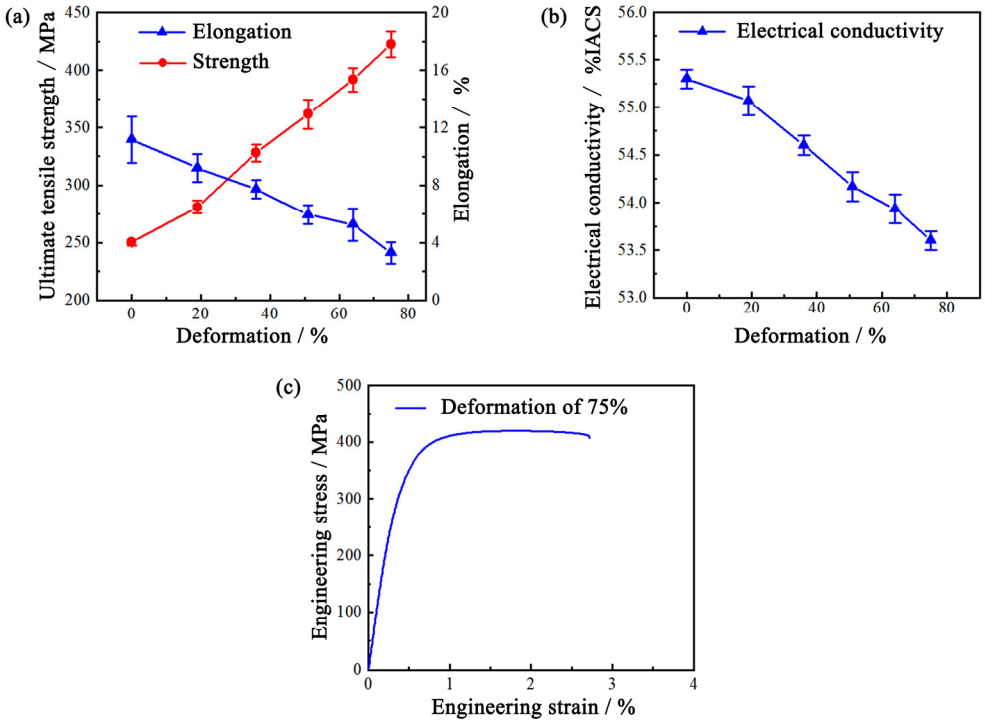

Figure 11. (**a**) Ultimate tensile strength, elongation, (**b**) electrical conductivity and (**c**) engineering stress–engineering strain curves of the composite wires after different numbers of passes of drawing deformation.

4. Discussion

4.1. Strengthening Mechanism of the Composite Wire During the Aging Process

After aging at 450 °C for 60 min, the Cu–Ni–Si alloy exhibited a deformed structure. Therefore, the yield strength of the Cu–Ni–Si alloy was determined by considering precipitation strengthening and dislocation strengthening. To simplify the calculation, all of the Ni and Si atoms were assumed to have precipitated in the form of δ-Ni_2Si. Table 3 provides the parameters used in the yield strength determination, taking into account different strengthening mechanisms.

Table 3. Parameters used in the yield strength calculations for the Cu–Ni–Si alloy.

Parameter	Description	Value	Units	Ref.
M	Taylor factor	3.06	-	[11]
b	Burgers vector of the Cu matrix	0.255	nm	[11,17,18]
G_{Cu}	Shear modulus of the Cu matrix	46	GPa	[11]
d_p	Average radius of the precipitates (450 °C/60 min)	7.2	nm	This work
f	Volume fraction of the precipitates	0.25%	-	This work
a	Constant	0.2	-	[11,17,18]

The increase in yield strength resulting from the precipitates can be calculated via the following equation [11,17,18]:

$$\Delta\sigma_p = 0.81 \times \frac{M \cdot G \cdot b}{2 \cdot \pi(1-\nu)^{1/2}} \times \frac{\ln(d_p/b)}{(\lambda - d_p)} \quad (1)$$

where M is the Taylor factor, b is the Burgers vector, G is the shear modulus, ν is Poisson's ratio, and λ is the spacing between particles in the glide plane. This spacing is related to

the radius d_p and the volume fraction f_v of the second-phase particles, as expressed in Equation (2) [11,17,18]:

$$\lambda = \frac{1}{2} d_p \sqrt{\frac{3\pi}{2f_v}} \quad (2)$$

The increase in yield strength resulting from dislocation strengthening can be calculated via Equation (3) [11,17,18].

$$\Delta\sigma_d = M\alpha G b\sqrt{\rho} \quad (3)$$

where M is the Taylor factor, α is a geometric constant, G is the shear modulus of the copper, b is the Burgers vector, and ρ is the dislocation density, which can be calculated using Equation (4) [11,17,18]:

$$\rho = \frac{16.1 \times \varepsilon^2}{b^2} \quad (4)$$

where ε is the microstrain and b is the Burgers vector.

Figure 12 shows the XRD pattern and the relationship between β cos (θ) and 4sin (θ) of the Cu–Ni–Si alloy after aging at 450 °C for 60 min. The dislocation density was calculated based on the height and width of the diffraction peaks, and the dislocation density of the Cu sample after aging at 450 °C for 60 min was 1.32×10^{14} m^{-2}. The properties of the Cu–Ni–Si alloy after aging at 450 °C for 60 min are displayed in Table 4.

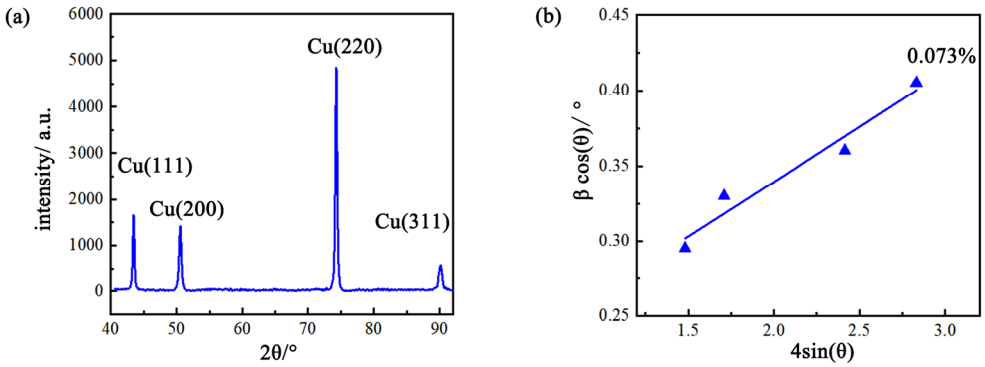

Figure 12. XRD pattern and the relationship between β cos (θ) and 4sin (θ) of the Cu–Ni–Si alloy after aging at 450 °C for 60 min: (**a**) XRD pattern and (**b**) the relationship between β cos (θ) and 4sin (θ).

Table 4. Calculated values of the increase in yield strength of the Cu–Ni–Si alloy via different strengthening mechanisms.

	Description	Strength	Units	Ref.
σ_0	Intrinsic lattice stress	52	MPa	[11,17,18]
σ_p	Precipitation strengthening	278	MPa	This work
σ_d	Dislocation strengthening	82	MPa	This work
σ_{total}	Total yield strength	412	MPa	This work

Precipitation and solid solutions of alloying elements rarely occur within the AA8030 alloy. Grain boundary strengthening and dislocation strengthening can be used to evaluate the influence of the microstructure of the AA8030 alloy on its properties. Table 5 provides the parameters used in the yield strength determination, taking into account different strengthening mechanisms.

Table 5. Parameters used in the yield strength calculation for the AA8030 alloy.

Parameter	Description	Value	Units	Ref.
M	Taylor factor	3.06	-	[21,22]
b	Burgers vector of the Al matrix	0.286	nm	[21,22]
G_{Al}	Shear modulus of the Al matrix	27.8	GPa	[21]
a	Constant	0.35	-	[21]
K_y	Hall–Petch constant	0.12	MPa·m$^{1/2}$	[22,23]

The increase in yield strength resulting from grain boundary strengthening can be calculated via Equation (5) [21–23]:

$$\sigma_{GB} = Kyd^{-1/2} \quad (5)$$

where K_y is the Hall–Petch constant and d represents the average grain diameter. Figure 13 shows the XRD pattern and the relationship between β cos (θ) and 4sin (θ) of the AA8030 alloy after annealing at 450 °C for 60 min. The dislocation density was calculated based on the height and width of the diffraction peaks, and the dislocation density of the Al alloy sample after aging at 450 °C for 60 min was 1.3 × 10^{13} m^{-2}. The properties of the AA8030 alloy after aging at 450 °C for 60 min are displayed in Table 6.

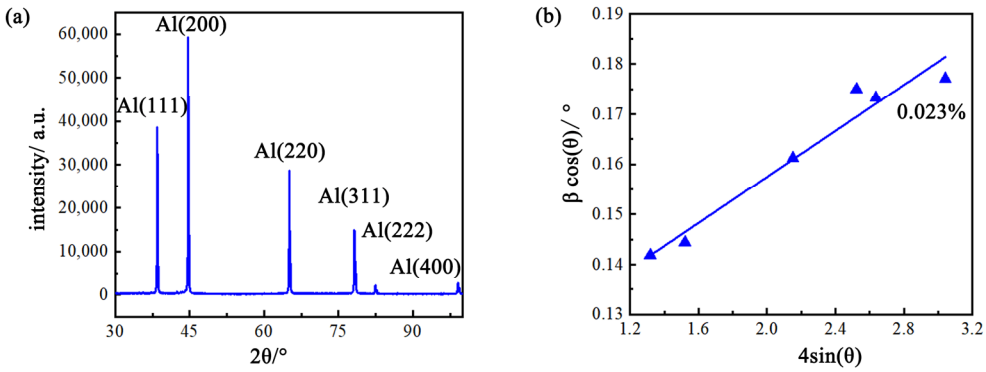

Figure 13. XRD and the relationship between β cos (θ) and 4sin (θ) of AA8030 alloy after annealing at 450 °C for 60 min: (**a**) XRD; (**b**) the relationship between β cos (θ) and 4sin (θ).

Table 6. Calculated increases in yield strength of the AA8030 alloy via different strengthening mechanisms.

	Description	Strength	Units	Ref.
σ_0	Intrinsic lattice stress	20	MPa	[21,22]
σ_{GB}	Grain boundary strengthening	33	MPa	This work
σ_d	Dislocation strengthening	19	MPa	This work
σ_{total}	Total yield strength	72	MPa	This work

The strength mixing rule is a commonly used method for analyzing the strength of a composite, and its calculation expression is presented as Equation (6) [24]:

$$\sigma_{CCA} = \sigma_{Cu}\, V_{Cu} + \sigma_{Al}\, V_{Al} \quad (6)$$

where σ represents the theoretical yield strength; V_{Cu} represents the volume fraction of the Cu alloy, which is 36% in this study; and V_{Al} represents the volume fraction of AA8030, which is 64% in this study. The yield strength of the composite wire was calculated via Equation (6) as 194.4 MPa. The calculated yield strength of the composite wire was very close to the experimental value (202 MPa), with an error of 3.7%.

On the basis of the above discussion, precipitation and dislocation strengthening played important roles in the aged Cu–Ni–Si alloy cladding, whereas grain boundary and dislocation strengthening contributed to the strength of the AA8030 alloy.

4.2. Detailed Analysis of Interfacial Layer Evolution During Aging and Deformation

To analyze the evolution mechanism of the composite interface during the aging process, EPMA and TEM were used to observe the interface of the composite wire after aging at 450 °C for 60 min. Figure 14a shows the elemental distribution at the interface, and Figure 14b–f show TEM bright-field images of the composite interface and the corresponding diffraction patterns. The TEM analysis further confirmed that the interface layer was composed of a Cu_9Al_4 layer, a CuAl layer and a $CuAl_2$ layer. Interestingly, the CuAl layer could be divided into two layers: the CuAl layer close to the Cu alloy and the CuAl layer close to the Al alloy. However, the Fe–Al phase could be found in the $CuAl_2$ layer and CuAl layer close to the Al alloy, and the Ni–Al phases were observed in the Cu_9Al_4 layer and CuAl layer close to the Cu alloy. The Fe–Al phase was the main second phase in the AA8030 alloy. Moreover, the Ni and Si in the Cu alloy precipitated and became enriched at the interface between the Cu_9Al_4 layer and the Cu alloy to form a Cu–Ni–Si phase.

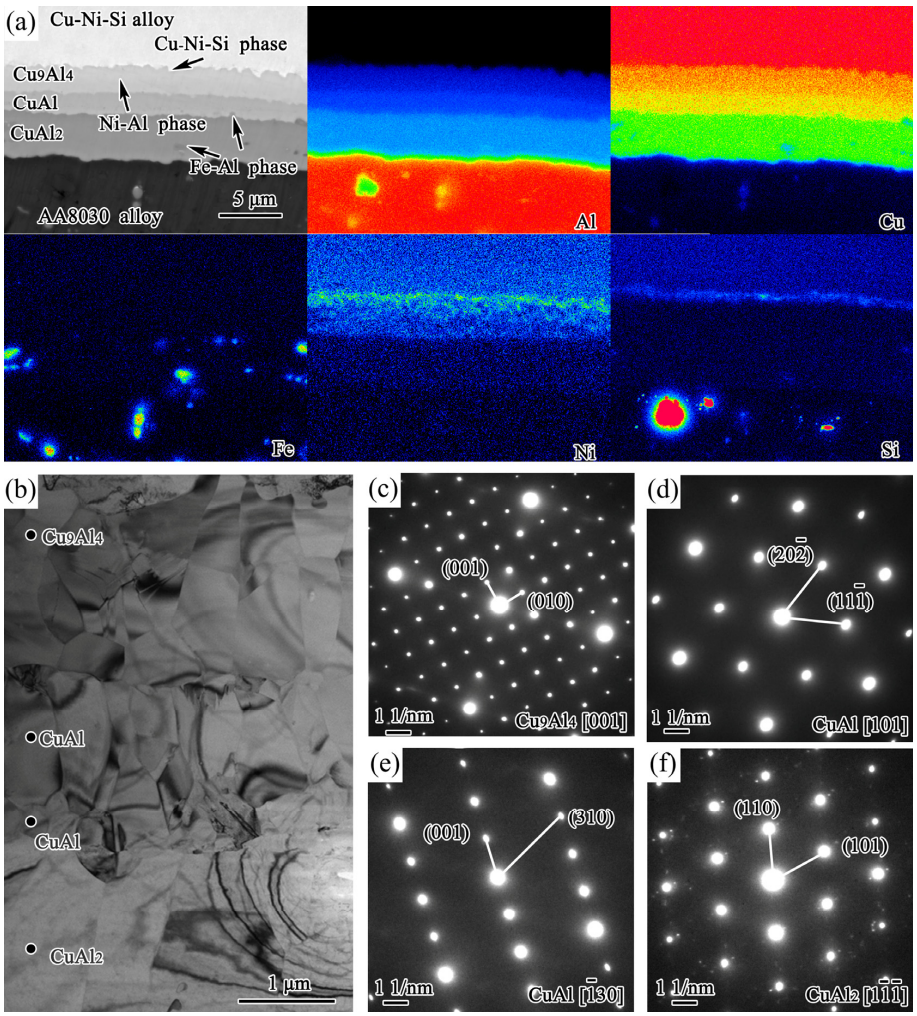

Figure 14. Analysis results of composite interface after heating at 450 °C for 60 min: (**a**) SEM morphology and EPMA mapping results; (**b**) TEM bright-field images of composite interface; (**c**) diffraction spot of the Cu_9Al_4 phase; (**d**,**e**) diffraction spot of the CuAl phase; (**f**) diffraction spot of the $CuAl_2$ phase.

To further characterize the crystal structures of the Fe–Al phase, Cu–Ni–Si phase and Ni–Al phase, further TEM and SAED analyses were performed. Figure 15a–c show TEM bright-field images of the Cu–Ni–Si phase, Ni-Al phase, and Fe-Al phase and the corresponding EDS results. Figure 15d shows a TEM high-resolution morphology image and the corresponding diffraction patterns of the Cu–Ni–Si phase. The Cu–Ni–Si phase can be identified as a $(Cu,Ni)_5Si$ phase with a cubic crystal structure and lattice constants a = b = c = 0.6301 nm [25]. Figure 15e shows a TEM high-resolution morphology image and the corresponding diffraction patterns of the Fe–Al phase. The Fe–Al phase can be identified as an $FeAl_3$ phase with a cubic crystal structure and lattice constants a = b = c = 0.6301 nm [26]. Figure 15f shows a diffraction pattern image of the Ni–Al phase. The Ni–Al phase can be identified as a Ni–Al phase with a cubic crystal structure and lattice constants a = b = c = 0.2887 nm [27,28].

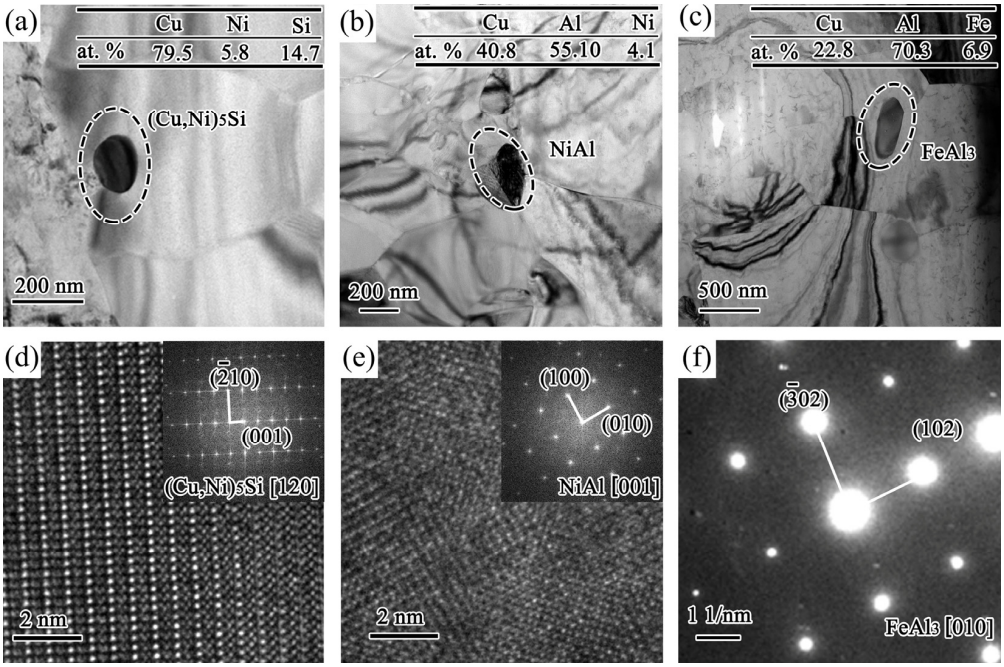

Figure 15. The analysis of different phases after heating at 450 °C for 60 min: (**a**–**c**) TEM bright-field images of (Cu, Ni)$_5$Si, NiAl and FeAl$_3$ phase and corresponding EDS result; (**d**) TEM high-resolution morphology and diffraction spot of the (Cu,Ni)$_5$Si phase; (**e**) TEM high-resolution morphology and diffraction spot of the NiAl phase; (**f**) diffraction spot of the FeAl$_3$ phase.

Based on the above experimental results, The $FeAl_3$ phase is the main second phase in AA8030 alloy, and the NiAl phases were formed in the Cu_9Al_4 layer and the CuAl layer close to the Cu alloy, so it can be deduced that the $CuAl_2$ layer and the CuAl layer close to the Al alloy grew towards the Al alloy side, while the Cu_9Al_4 layer and the CuAl layer close to the Cu alloy grew towards the Cu alloy side. Meanwhile, the Ni and Si elements in the Cu alloy precipitated at the interface between the Cu_9Al_4 layer and Cu alloy to form a $(Cu,Ni)_5Si$ phase.

On the basis of the above analysis, the interfacial layer after aging was composed primarily of $CuAl_2$, CuAl, and Cu_9Al_4, which are significantly harder than both the Al alloy and the Cu alloy. Fracture occurred during the subsequent drawing process. Figure 16 shows a schematic diagram of the interface evolution during the deformation process of the composite wire. When the deformation was relatively low (one pass, with a deformation of 19%), brittle fracture occurred within the interface layer, and new bonds formed. Under the pressure applied by the mold, the fractured interface layer began to deviate from the drawing direction, as illustrated in Figure 16a. As the deformation increased (two passes, with a deformation of 36%), the new bonds were gradually expanded, and the angle

between the fractured intermetallic compound and the drawing direction continued to increase under the pressure of the mold, as shown in Figure 16b.

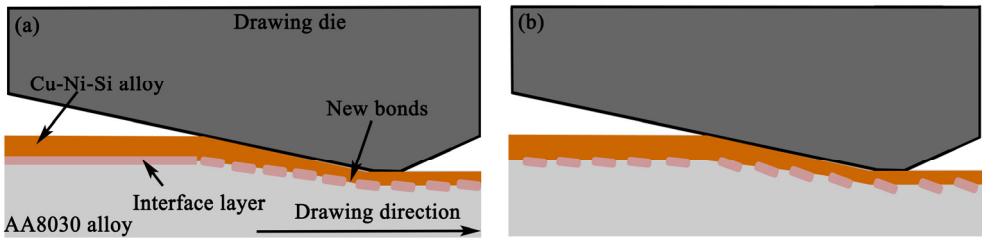

Figure 16. Schematic diagram of interface evolution during deformation process of composite wire: (**a**) one pass, with a deformation of 19%; (**b**) two passes, with a deformation of 36%.

5. Conclusions

In this study, the effects of aging and deformation parameters on the microstructure and properties of Cu–Ni–Si alloy/AA8030 alloy composite wires were investigated. The main conclusions are as follows:

(1) After aging at 450 °C for 60 min, the composite wire exhibited relatively high comprehensive properties, with ultimate tensile strength, elongation, and electrical conductivity values of 253 MPa, 11.1%, and 55.3% IACS, respectively. In this state, the AA8030 alloy exhibited recrystallized structures, and the hardness decreased to approximately 40 HV. Moreover, Ni_2Si phases with an average size of approximately 7.2 nm were formed within the Cu–Ni–Si alloy, which increased the hardness of the Cu–Ni–Si alloy to 150.3 HV.

(2) After five drawing passes (with a deformation of 75%), the ultimate tensile strength, elongation and electrical conductivity of the composite wire were 422 MPa, 3.3%, and 53.6% IACS, respectively. As the deformation increased, the dislocation density of the AA8030 alloy and Cu–Ni–Si alloy gradually increased, and the dislocation strengthening effect significantly improved.

(3) After aging, the interface layer was composed of a $CuAl_2$ layer, a CuAl layer and a Cu_9Al_4 layer. The $CuAl_2$ and Cu_9Al_4 layers grew toward the Al alloy and Cu alloy, respectively, whereas the CuAl layer grew toward both the Al alloy and the Cu alloy.

Author Contributions: Conceptualization, F.Z. and X.L.; Methodology, S.T. and F.Z.; Software, S.T.; Formal analysis, S.T.; Investigation, S.T.; Data curation, S.T.; Writing – original draft, S.T.; Writing – review & editing, F.Z. and X.L.; Supervision, X.L.; Funding acquisition, F.Z. and X.L. All authors have read and agreed to the published version of the manuscript.

Funding: This research was supported by the National Key Research and Development Program of China (grant number: 2018YFA0707303), the National Natural Science Foundation of China (grant number: 51925401) and the Young Elite Scientists Sponsorship Program by CAST (grant number: 2022QNRC001).

Data Availability Statement: The original contributions presented in the study are included in the article, further inquiries can be directed to the corresponding authors.

Conflicts of Interest: The authors declare no conflict of interest.

References

1. Pintore, M.; Mittler, T.; Volk, W.; Starykov, O.; Tonn, B. Experimental investigations on the influence of the thermal conditions during composite casting on the microstructure of Cu-Al bilayer compounds. *Int. J. Met.* **2018**, *12*, 79–88. [CrossRef]
2. Chang, D.; Wang, P.; Zhao, Y. Effects of asymmetry and annealing on interfacial microstructure and mechanical properties of Cu/Al laminated composite fabricated by asymmetrical roll bonding. *J. Alloys Compd.* **2020**, *815*, 152453. [CrossRef]
3. Wang, Y.; Song, R.; Yanagimoto, J.; Li, H. Effect of heat treatment on bonding mechanism and mechanical properties of high strength Cu/Al/Cu clad composite. *J. Alloys Compd.* **2019**, *801*, 573–580. [CrossRef]

4. Mao, Z.; Xie, J.; Wang, A.; Wang, W.Y.; Ma, D.Q.; Liu, P. Effects of annealing temperature on the interfacial microstructure and bonding strength of Cu/Al clad sheets produced by twin-roll casting and rolling. *J. Mater. Process. Technol.* **2020**, *285*, 116804. [CrossRef]
5. Zhang, J.P.; Huang, H.G.; Sun, J.N.; Zhao, R.D.; Feng, M. Interfacial pressure distribution and bonding characteristics in twin-roll casting of Cu/Al clad strip. *Trans. Nonferrous Met. Soc. China* **2022**, *32*, 2965–2978. [CrossRef]
6. Bakke, A.O.; Arnberg, L.; Li, Y. Achieving high-strength metallurgical bonding between A356 aluminum and copper through compound casting. *Mater. Sci. Eng. A* **2021**, *810*, 140979. [CrossRef]
7. Wan, T.; Li, S.; Ren, Z.; Han, J.C.; Huang, Q.X. A novel approach for preparing Cu/Al laminated composite based on corrugated roll. *Mater. Lett.* **2019**, *234*, 79–82.
8. Shan, Y.Q.; Zhang, C.M.; Zhang, Y.M.; Feng, J.; Zhao, S.H.; Huang, B.H.; Song, K.X.; Zhou, Y.J. Influence of different rolling passes and deformation amounts on the microstructure evolution and strengthening mechanism of Cu-Ni-Si alloy. *J. Mater. Res. Technol.* **2024**, *33*, 3205–3220. [CrossRef]
9. Shan, Y.Q.; Zhang, Y.M.; Zhang, C.M.; Feng, J.; Huang, B.H.; Zhao, S.H.; Song, K.X. Study on the microstructure and mechanism of stress relaxation behavior of Cu–Ni–Si alloy by two-stage rolling deformation. *Mater. Sci. Eng. A* **2024**, *908*, 146946. [CrossRef]
10. Lu, L.; Ding, Z.M.; Zhang, M.X.; Song, H.W.; Deng, S.Y.; Zhang, S.H. Effect of continuous extrusion forming on mechanical properties of aged Cu-Ni-Si alloy. *Mater. Today Commun.* **2024**, *39*, 108858. [CrossRef]
11. Lei, Q.; Xiao, Z.; Hu, W.; Derby, B.; Li, Z. Phase transformation behaviors and properties of a high strength Cu-Ni-Si alloy. *Mater. Sci. Eng. A* **2017**, *697*, 37–47. [CrossRef]
12. Pan, L.; Liu, K.; Breton, F. Effect of Fe on Microstructure and Properties of 8xxx Aluminum Conductor Alloys. *J. Mater. Eng. Perform.* **2016**, *25*, 5201–5208. [CrossRef]
13. Chen, P.; Fan, X.; Yang, Q.; Zhang, Z.; Jia, Z.; Liu, Q. Creep behavior and microstructural evolution of 8030 aluminum alloys compressed at intermediate temperature. *J. Mater. Res. Technol.* **2021**, *12*, 1755–1761. [CrossRef]
14. Jiang, X.; Zhang, Y.; Yi, D.; Wang, H.S.; Deng, X.B. Low-temperature creep behavior and microstructural evolution of 8030 aluminum cables. *Mater. Charact.* **2017**, *130*, 181–187. [CrossRef]
15. Guo, Y.; Yi, D.; Liu, H.; Wang, B.; Jiang, B.; Wang, H.S. Mechanical properties and conductivity of graphene/Al-8030 composites with directional distribution of graphene. *J. Mater. Sci.* **2020**, *55*, 3314–3328. [CrossRef]
16. Tian, S.K.; Zhao, F.; Liu, X.H. Evolution of microstructure and properties in Cu-Ni-Si alloy clad AA8030 alloy composites prepared by continuous casting composite technology with gradient-varying drawing speeds. *Mater. Today Commun.* **2024**, *40*, 109802. [CrossRef]
17. Liao, W.; Liu, X.; Yang, Y. Relationship and mechanism between double cold rolling-aging process, microstructure and properties of Cu-Ni-Si alloy prepared by two-phase zone continuous casting. *Mater. Sci. Eng. A* **2020**, *797*, 140148. [CrossRef]
18. Liao, W.; Liu, X.; Liu, Q. High strength and high electrical conductivity C70250 copper alloy with fibrous structure reinforced by high density, multi-scale nano-precipitates and dislocation. *Mater. Sci. Eng. A* **2022**, *846*, 143283. [CrossRef]
19. Liu, W.C.; Morris, J.G. Evolution of recrystallization and recrystallization texture in continuous-cast AA3015 aluminum alloy. *Metall. Mater. Trans. A Phys. Metall. Mater. Sci.* **2005**, *36*, 2829–2848. [CrossRef]
20. Hug, E.; Bellido, N. Brittleness study of intermetallic (Cu, Al) layers in copper-clad aluminium thin wires. *Mater. Sci. Eng. A* **2011**, *528*, 7103–7106. [CrossRef]
21. Liu, F.; Liu, Z.Y.; He, G.Y.; Ou, L.N. Dislocation ordering and texture strengthening of naturally aged Al-Cu-Mg alloy. *J. Mater. Sci. Technol.* **2022**, *118*, 1–14. [CrossRef]
22. Jiang, L.; Wang, C.; Fu, H.; Shen, J.; Zhang, Z.; Xie, J. Discovery of aluminum alloys with ultra-strength and high-toughness via a property-oriented design strategy. *J. Mater. Sci. Technol.* **2022**, *98*, 33–43. [CrossRef]
23. Huang, K.; Engler, O.; Li, Y.J.; Marthinsen, K. Evolution in microstructure and properties during non-isothermal annealing of a cold-rolled Al-Mn-Fe-Si alloy with different microchemistry states. *Mater. Sci. Eng. A* **2015**, *628*, 216–229. [CrossRef]
24. Chen, K.; Yu, H.; Hu, X. Simulation of room-temperature strength of ZA22/Al_2O_3(F) composites. *Acta Metall. Sin.* **1997**, *33*, 437–442.
25. Mattern, N.; Seyrich, R.; Wilde, L.; Baehtz, C.; Knapp, M.; Acker, J. Phase formation of rapidly quenched Cu–Si alloys. *J. Alloys Compd.* **2007**, *429*, 211–215. [CrossRef]
26. Zhang, N.F.; Hu, Q.D.; Ding, Z.Y.; Lu, W.; Yang, F.; Li, J. 3D morphological evolution and growth mechanism of proeutectic $FeAl_3$ phases formed at Al/Fe interface under different cooling rates. *J. Mater. Sci. Technol.* **2022**, *16*, 83–93. [CrossRef]
27. Choudhuri, D.; Banerjee, R.; Srinivasan, S.G. Uniaxial deformation of face-centered-cubic(Ni)-ordered B_2(NiAl) bicrystals: Atomistic mechanisms near a kurdjumov-sachs interface. *J. Mater. Sci.* **2018**, *53*, 5684–5695. [CrossRef]
28. Tian, S.; Zhao, F.; Liu, X. Clarification of the solid-state diffusion behavior of a copper alloy/aluminum alloy composite interface assisted by position marking of the second phases. *Mater. Charact.* **2022**, *192*, 112173. [CrossRef]